Chemical Engineering Journal 529 (2026) 172970

Contents lists available at ScienceDirect

Chemical Engineering Journal

journal homepage: www.elsevier.com/locate/cej

Fine-tuned Ce electron density directs H_2O_2 activation pathway in industrially employable CeO_2 nanozymes for ~100% specificity and boosted activity in (Bromo)peroxidase mimicking

Tianqi Cheng [a,1], Bo Yuan [a,*,1], Chao Zhao [a,1], Zicong Tan [b,c,**], Xinyu Wu [a,d], Jian Lin Chen [d], Juan Liu [b,c], Yufei Zhao [e], Hui Wei [f,*], Yung-Kang Peng [a,*]

[a] Department of Chemistry, City University of Hong Kong, 999077, Hong Kong
[b] School of Environmental Science and Engineering, Guangzhou University, Guangzhou, 510006, China
[c] Key Laboratory of Waters Safety & Protection in the Pearl River Delta, Ministry of Education, Guangzhou, 510006, China
[d] Department of Applied Science, School of Science and Technology, Hong Kong Metropolitan University, 999077, Hong Kong
[e] State Key Laboratory of Chemical Resource Engineering, Beijing University of Chemical Technology, Beijing, 100029, China
[f] Department of Biomedical Engineering, College of Engineering and Applied Sciences, Nanjing National Laboratory of Microstructures, Jiangsu Key Laboratory of Artificial Functional Materials, Nanjing University, Nanjing, Jiangsu, 210023, China

ARTICLE INFO

Keywords:
CeO_2 nanozymes
H_2O_2 activation
Reaction specificity
(bromo)peroxidase mimicry
Cost-effective
Scalable production

ABSTRACT

Nanozymes are promising alternatives to natural enzymes; however, most of them lack specificity, resulting in multiple enzyme-like activities that can interfere with one another in targeted applications. For example, CeO_2 nanozymes are often reported to exhibit both peroxidase (POD)-like and bromoperoxidase (BPO)-like activities. However, H_2O_2 inevitably competes in these reactions, reducing its utilization and performance in respective applications. Herein, we present a facile and scalable method for producing CeO_2 nanozymes with controllable reaction specificity. By adjusting the preparation atmospheres, the presence/ absence of coordinated N species allows for tuning the electron density of Ce sites, resulting in distinct H_2O_2 activation pathways and enabling nearly 100% mimicry of POD- and BPO-like activity. The absence of interference from one activity was demonstrated to intrinsically boost the other activity of CeO_2 nanozymes by over 1000%, far exceeding improvements reported in the literature. Additionally, our approach eliminates the need for labor-intensive purification, making it more cost-effective than natural enzymes and suitable for large-scale use. The optimized samples were then used to illustrate the importance of specificity control in enhancing performance for glucose detection and anti-bacterial/fouling applications. This work thus marks a milestone in artificial enzyme development, paving the way for the practical application of nanozymes.

1. Introduction

Nanomaterials that catalyze enzymatic reactions, known as nanozymes, have emerged as a promising alternative to natural enzymes due to their greater pH/thermal stability at a lower cost [1–3]. This field has rapidly expanded in recent years, with potential applications in therapy, food preservation, environmental remediation, and sensor development [4–7]. However, most nanozymes are not designed to mimic the specific mechanisms of natural enzymes, resulting in multiple enzyme-like activities [8–10]. While this diversity enables self-cascade reactions in some therapeutic contexts [4], the lack of substrate/reaction specificity can hinder performance in targeted applications due to unavoidable interferences [11,12]. Taking H_2O_2, the most common substrate, as an example: peroxidase (POD) uses it to oxidize 3,3′,5,5′-tetramethylbenzidine (TMB) (Scheme 1a(i)), while bromoperoxidase (BPO) employs it to oxidize bromide (Br^-) to hypobromous acid (HOBr) (Scheme 1a(ii)). Since they do not catalyze each other's reactions, there is no competition for H_2O_2, ensuring optimal performance in their respective applications such as biomolecule sensing for POD [13] and antibacterial/fouling for BPO [14]. However, for nanozymes that exhibit

* Corresponding authors.
** Correspondence to: Z. Tan, School of Environmental Science and Engineering, Guangzhou University, Guangzhou, 510006, China.
E-mail addresses: boyuan8@cityu.edu.hk (B. Yuan), zicong.tan@gzhu.edu.cn (Z. Tan), weihui@nju.edu.cn (H. Wei), ykpeng@cityu.edu.hk (Y.-K. Peng).
[1] These authors contribute equally to this work.

https://doi.org/10.1016/j.cej.2026.172970
Received 23 October 2025; Received in revised form 25 December 2025; Accepted 12 January 2026
Available online 19 January 2026

both activities, H_2O_2 is inevitably consumed in both reactions (see discussion below), leading to suboptimal performance in the targeted applications.

Mechanistic studies reveal that the POD-like activity of nanozymes is closely linked to their ability to convert H_2O_2 into OH radicals via a so-called "radical pathway" [15]. As shown in Scheme 1b(i), the reduction of H_2O_2 by M^{n+} generates OH radicals (step I), which subsequently produce TMB_{ox} (step II) for color change and HO_2 radicals (step III) for M^{n+} regeneration (step IV). Since step I is rate-limiting, nanozymes that can rapidly reduce H_2O_2 thus exhibit higher POD-like activity, with their reaction rate positively correlated to the electron richness of the active sites [16–18]. In contrast, when H_2O_2 interacts with active sites that have limited redox capability (or those in high oxidation states), it forms surface peroxo species instead (Scheme 1b(ii)). The reactivity of these species is correlated, in an opposing manner, to the electron deficiency (or Lewis acidity) of the active sites [19–21]. Although H_2O_2 activation via this "peroxo pathway" is often employed in heterogeneous catalysis for selective oxidation, it has rarely been explored in nanozymes. Pioneered by Herget et al. [22], the mimicry of BPO by CeO_2 was first attributed to the formation of surface Ce-peroxo species for Br^- oxidation, as OH radicals do not produce HOBr when reacting with Br^- [23].

In the literature, it is often concluded that a high Ce^{3+}/Ce^{4+} ratio in CeO_2 nanozymes enhances both POD-like [24,25] and BPO-like [26–29] activities. However, a single factor is unlikely to activate H_2O_2 through a different pathway. In our opinion, this discrepancy stems from the limitations of commercial X-ray photoelectron spectroscopy (XPS) often used for catalytic correlation. For example, Ce_{3d} XPS only provides discrete electronic states (Ce^{3+} or Ce^{4+}), failing to reveal the continuous changes in Ce electron density with its local environment. Recently, our group addressed these limitations using probe-assisted nuclear magnetic resonance (NMR) [30,31]. We found that the dual mimicking activities in CeO_2 nanozymes are closely linked to surface Ce sites with medium electron density [32]. These sites slowly convert H_2O_2 via both pathways into OH radicals and HOBr (Scheme 1c(i)), resulting in poor POD-like and BPO-like activities. Since OH radicals can decompose free H_2O_2, their presence further limits H_2O_2 utilization in BPO-like activity (and vice versa for peroxo species formation in POD-like activity). Such interference suggests that the observed POD/BPO-like activity of nanozymes in the literature [24–29] could be suboptimal if the alternate pathway is not fully suppressed.

To address this issue, as informed by the mechanisms (Scheme 1b), one can adjust the electron density of the active sites—either to sufficiently high or low levels—to minimize interference from one activity while increasing the other [33]. In other words, enzymatic specificity and activity can be improved simultaneously by properly tuning the electron density of the active sites. Although some reported surface modification methods [33–38] may unintentionally regulate this property to enhance enzymatic specificity/activity, their preparation protocols are complex, requiring precursor synthesis, multi-step processes, and long reaction times (see Table S1 for detailed comparison). Additionally, the need for repeated centrifugation and washing during sample purification significantly increases labor intensity. This, combined with limited yields (mostly at the milligram scale), results in high preparation costs and severely restricts their practical applications. Therefore, it is highly desirable to develop cost-effective, scalable nanozymes with the required electron density to engage in the targeted H_2O_2 activation pathway for optimal POD/BPO-like activities in specific applications [39].

Herein, we present a facile method for preparing ultrasmall CeO_2 nanoparticles (NPs) embedded in a carbon-based framework by calcining a mixture of Ce precursor and polyvinylpyrrolidone (PVP) (Scheme 1c(ii)). The resulting sample requires no purification, making them suitable for large-scale production at minimal cost. Most importantly, the mimicry of POD/BPO can be easily regulated by adjusting the preparation atmospheres (N_2/air), achieving high activity and nearly 100% specificity. This contrasts sharply with typical CeO_2 NPs, which display dual but poor POD- and BPO-like activities because of competition for H_2O_2. Surface analysis reveals that N_2-prepared samples have high electron density in surface Ce sites due to the formation of Ce—N species, enabling rapid reduction of H_2O_2 to OH radicals and resulting in exclusive POD-like activity. In contrast, this radical pathway is suppressed in air-prepared samples, where the species is removed, creating electron-lean Ce sites with high Lewis acidity. Consequently, the as-formed Ce-peroxo species selectively oxidize Br^- to HOBr, leading to dominant BPO-like activity. The optimized samples under N_2/air conditions show significantly different performances in glucose detection and antibacterial/fouling applications. This highlights the critical importance of regulating active site electron density for specificity control and optimal performance, even in pristine material.

2. Experimental section

2.1. Synthesis of the samples

Polyvinylpyrrolidone (PVP, Mw = 1300,000) and $Ce(NO_3)_3{\cdot}6H_2O$ were pre-mixed in DI water at a weight ratio of 1:1.5. The mixture was

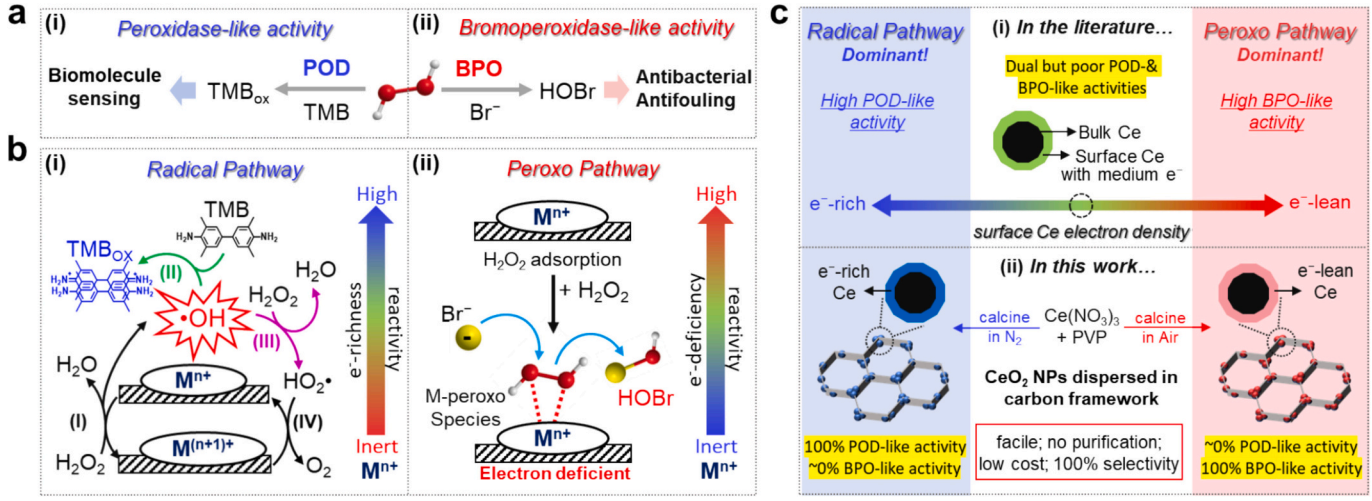

Scheme 1. Schematic illustration of (a) enzymatic reactions performed by (i) POD and (ii) BPO, and (b) H_2O_2 activation via (i) the radical pathway for POD mimicking and (ii) the peroxo pathway for BPO mimicking. (c) Control of H_2O_2 activation and reaction specificity in CeO_2-based nanozymes with Ce electron density analysis from (i) the literature [32] and (ii) this work.

heated to 70 °C and magnetically stirred for 30 min to ensure complete dissolution and uniform mixing. The resulting solution was then transferred into the crucible for the calcination under various atmospheres and temperatures. Air-calcined samples were synthesized in a muffle furnace, while N_2-calcined samples were prepared in a tube furnace with a nitrogen flow of 100 mL/min. Both calcination protocols involved heating at a rate of 5 °C per minute to the target temperature, maintaining that temperature for 30 min, and then allowing the samples to cool naturally to room temperature within the furnace. The resulting samples can directly be used without purification.

2.2. Peroxidase (POD)-like activity of the samples

The POD-like activity of samples was tested with 3,3′,5,5'-Tetramethylbenzidine (TMB) as an indicator in acidic solution (pH = 4.0) at room temperature. Each measurement was conducted with a final volume of 1.5 mL in the cuvette, involving 1 mg/mL catalyst dispersion (100 μL), 1 mM H_2O_2, and 0.5 mM TMB. The final concentration of the catalyst was calculated to be 66.7 μg/mL. UV–vis spectroscopy was used to record absorption scans at 1-min intervals for a total of 20 min. The product TMB_{ox} can be detected by the evolution of the peak at 652 nm (ε_{652} = 39,000 M^{-1} cm^{-1}).

2.3. Bromoperoxidase (BPO)-like activity of the samples

The phenol red bromination assay was used to investigate the BPO-like activity of samples. 1 mg/mL catalyst dispersion (100 μL), 1 mM H_2O_2, 25 mM KBr, and 0.04 mM phenol red were employed in the reaction system with a total volume of 1.5 mL. The final concentration of the catalyst was calculated to be 66.7 μg/mL. UV–vis spectroscopy was recorded at 1-min intervals for a total of 20 min. The absorbance of phenol red (PR) and bromophenol blue (Br_4PR) was measured at 430 nm (ε_{430} = 23,900 M^{-1} cm^{-1}) and 590 nm (ε_{590} = 72,200 M^{-1} cm^{-1}), respectively.

2.4. Activity and kinetic study of POD and BPO

Due to the high reactivity of natural enzymes, 0.0075 U/mL (or 0.05 μg/mL) of POD was used to evaluate its capability in TMB oxidation with H_2O_2, while keeping all other experimental conditions consistent with those for its mimetics. Similarly, for assessing BPO's capability in HOBr production with H_2O_2, 0.02 U/mL (or 0.2 μg/mL) of BPO was employed, with all other conditions unchanged from those used for its mimetics. Under these conditions, the k constants for POD and BPO were calculated to be 5.40×10^{-3} and 24.04×10^{-3} min^{-1}, respectively. Since the amounts of POD and BPO used in the reactions were much lower than those in our samples, their rate constants were further normalized to facilitate a fair comparison. Since 66.7 μg/mL of catalysts was used to evaluate their POD-like and BPO-like activities above (see Sections 2.2 and 2.3), the normalized k constant for POD was thus calculated as follows: 5.40×10^{-3} min^{-1} × (66.7 μg/mL ÷ 0.05 μg/mL) = 7203.60 × 10^{-3} min^{-1}. Similarly, the normalized k constant for BPO was determined as:

$$24.04 \times 10^{-3}\ \text{min}^{-1} \times (66.7\ \mu\text{g/mL} \div 0.2\ \mu\text{g/mL}) = 8017.34 \times 10^{-3}\ \text{min}^{-1}$$

2.5. Infrared (IR) surface study with pyridine

Firstly, 20 mg samples were pre-treated at 120 °C in furnace for 24 h to remove surface adsorbed water. Then, 1 mL of pyridine solution was introduced after samples naturally cooling to 60 °C. Subsequent sonication (for 30–60 s) was conducted to ensure the complete adsorption of pyridine on active sites. The resulting mixture was heated to 90 °C to remove the unabsorbed pyridine. Finally, the IR spectra were collected under attenuated total reflectance (ATR) mode with the IR spectrometer.

2.6. Nuclear magnetic resonance (NMR) surface study with trimethyl phosphine oxide (TMPO)

Prior to TMPO adsorption, samples (100 mg) were subjected to surface cleaning at 373 K under a vacuum of 10^{-1} Pa. For probe molecule adsorption, the cleaned samples were combined with a 0.1 M TMPO solution in CH_2Cl_2 and allowed to interact. The resulting TMPO-adsorbed samples were subsequently dried under vacuum conditions. Room-temperature ^{31}P NMR spectroscopy was performed using an Agilent 600 M spectrometer, with chemical shifts calibrated against an external 85% H_3PO_4 aqueous reference.

2.7. Electron paramagnetic resonance (EPR) detection of OH radicals

EPR measurements were carried out in ambient condition on ADANI SpinscanX spectrometer operating at 100 kHz field modulation at room temperature. 5,5-dimethyl-1-pyrroline N-oxide (DMPO) was selected as the radical trapper for the detection of OH radicals. Typically, 100 μg samples and 5 μL of DMPO were dispersed in the 1 mL of solution with freshly prepared 100 mM H_2O_2. The mixture was allowed to react for 10 min. Subsequently, the supernatant obtained through centrifugation with the removal of samples was used for the detection of OH radicals.

2.8. Disproportionation of H_2O_2

The assessment of H_2O_2 disproportionation was performed by dispersing 1000 μg of samples in 15 mL of reaction solution containing 50 mM H_2O_2 with or without 100 mM KBr in the centrifuge tubes at room temperature. Continuous stirring was conducted to prevent the sample agglomeration. Every 1.5 mL of supernatant was collected by centrifugation to avoid the interference of samples at intervals of 30 min for 120 min. The H_2O_2 decomposition was monitored at 240 nm using UV–vis spectroscopy (ε_{240} = 39.4 M^{-1} cm^{-1}).

2.9. Raman study of the dynamic changes in the O—O bond of H_2O_2

Raman spectrometer (Bayspec Agility, excitation wavelength λ = 785 nm) was employed to track the dynamic changes of the O—O bond of H_2O_2 on catalysts. For the measurements, 5 mg of catalyst was pressed into a wafer and placed on a sample holder. The reaction was initiated by adding a 5 μL droplet of 5 M H_2O_2 (with or without 250 mM KBr) onto the catalyst. Raman signals were recorded at the specified time.

2.10. Temperature and pH stability study

Stability study was conducted by incubating N-600, A-400, peroxidase, and bromoperoxidase in different temperatures (from 0 °C to 65 °C) or pH conditions (from 3 to 14, adjusted using acetate buffer solution, PIPES buffer solution, PBS buffer solution, and NaOH solution) for 120 min and then testing their activities under the same conditions as that of peroxidase-like and bromoperoxidase-like activity study. For POD-like reaction, 0.0075 U/mL of POD was used, while 0.02 U/mL BPO was added to the reaction solution for BPO-like activity detection. All the reactions were assessed at room temperature.

2.11. Density functional theory (DFT) computation

The spin-polarized DFT computation was performed using the Quantum Espresso package with plane-wave pseudopotential approach [40–43]. To calculate the exchange and correlation energies, the Perdew-Burke-Ernzerhof (PBE) generalized gradient approximation (GGA) density functional was employed [44]. The Hubbard correction of U = 3.125 eV was applied to the Ce 4*f* orbitals according to previous studies to balance the efficiency and accuracy [45,46]. A convergence

test on the cut-off energy (E_{cutoff}) for the plane waves ranging from 30 to 70 Ry at intervals of 5 Ry and showed that the total energy (eV/atom) converges to approximately −188.572 when the E_{cutoff} exceeds 50 Ry, with ΔE remaining below 1 meV/atom (Fig. S1). The cut-off energy for the plane waves was 50 Ry and the structure was relaxed until the total force was less than 0.02 eV/Å. The conventional cell of CeO_2 was optimized with k-points of 6 × 6 × 6, which enlarge the lattice constant from 5.411 to 5.494 Å. A 2 × 2 slab model was used to simulate the pristine (111) and N-doped (111) (i.e. N-(111)) surface, where 1/4 surface oxygen atom is replaced by nitrogen atom (Fig. S2). The vacuum layer of these models was 15 Å, and the shadowed atoms at the bottom were fixed. The adsorption energies for H_2O_2 and Br are calculated as below:

$$E_{ads.} = E_{all} - (E_{slab} + E_{adsorbate})$$

where E_{all} represents the energy of the system after the adsorption of adsorbate while E_{slab} and $E_{adsorbate}$ represent the energies for the pristine surface and the free adsorbate (e.g., H_2O_2/Br). For the solvent effect, the implicit solvent effect was taken into account by using ENVIRON module (http://www.quantum-environ.org) implemented in Quantum Espresso. The following parameters were used to simulate solvent effect of water: env_static_permittivity = 78.3, env_pressure = −0.35 GPa, env_surface_tension = 50 dyn/cm, rhomax = 0.005 a.u., rhomin = 0.0001 a.u [47]. The free energy for the key intermediate species in POD and HPO pathway were calculated at 298 K using phonopy package [48].

2.12. Glucose detection

For glucose detection, glucose solution with different concentrations (0.001, 0.002, 0.005, 0.008, 0.01, 0.02, 0.05, 0.08, 0.1, 0.2, 0.5, 1, 2 mM) was first prepared. 650 μL of this solution was allowed to react with 100 μL of GO_x (1 mg/mL) for 30 min at 37 °C. After incubation, 100 μL of N-600/A-400 dispersion (1 mg/mL), 150 μL of TMB (5 mM), and 500 μL of acidic buffer (pH = 4.0) were introduced into the solution to react for 15 min. The absorbance of TMB_{ox} at 652 nm in resulting supernatant was recorded with UV–vis spectroscopy. Selectivity test was conducted by replacing glucose with 20 mM of interfering agents including Na^+, K^+, maltose, sucrose, fructose, L-arginine, and L-valine under the same experimental procedure.

2.13. Glucose detection in serum samples

650 μL of the serum samples (the fetal bovine serum sample was diluted by PBS buffer before use) were mixed with 100 μL of glucose oxidase (1 mg/mL) and incubated for 30 min at 37 °C. The resulting solution was allowed to react with 100 μL of N-600 dispersion (1 mg/mL), 150 μL of TMB (5 mM), and 500 μL of acidic buffer (pH = 4.0) for 15 min. The absorbance of TMB_{ox} (652 nm) in supernatant was recorded with UV–vis spectroscopy.

2.14. Antibacterial performance

The antibacterial activity of N-600 and A-400 against *E. coli* was evaluated using the standard plate counts test. The samples of 1.5 mM were pre-mixed with 0.4 mM H_2O_2 and 2 mM KBr, and subsequently incubated with *E. coli* suspension at 37 °C for 15 min. After incubation, 100 μL of the suspensions were plated on Lysogeny broth agar plates and incubated at 37 °C for 18 h. For scanning electron microscopy imaging, *E. coli* suspensions with different treatments were collected, fixed with 2.5% glutaraldehyde, dehydrated with ethanol, and placed on a silicon wafer. Bacterial morphology was characterized using a Thermo Scientific Quattro ESEM instrument at 15.0 kV. *E. coli* expressing green fluorescent protein (GFP-*E. coli*) was used for measuring the performance of N-600 and A-400 as antibacterial coating on stainless steel slices. After incubated in the GFP-*E. coli* suspension (with 2 mM of Br^- and 0.4 mM of H_2O_2) for 7 days at 37 °C, the treated slices were conducted with confocal analysis using a Nikon Spinning Disk Confocal Imaging System.

3. Results and discussion

3.1. Preparation and characterization

CeO_2-based nanozymes with controllable POD- and BPO-like activity were synthesized by calcining a mixture of $Ce(NO_3)_3$ and PVP (denoted as $Ce(NO_3)_3$-PVP) using nitrogen, the most economical inert gas, and air as the calcination atmospheres. The resulting samples are labeled N/A-X, where N/A indicates the calcination atmosphere (N_2/air) and X denotes the temperature. Taking the sample prepared at 500 °C as an example, both N-500 and A-500 exhibit a porous framework with strong C, Ce, O signals (cf. N signal) uniformly distributed within the framework (Fig. 1a). Transmission electron microscopy (TEM) images reveal that spherical NPs are densely dispersed in the framework of the samples (Fig. 1b). Their average sizes are similar, measuring 4.28 ± 0.60 nm for N-500 and 4.83 ± 0.66 nm for A-500 (Fig. S3). X-ray diffraction (XRD) confirms these particles as CeO_2 (Fig. 1c), with sizes aligning with Scherrer equation predictions based on the (111) diffraction peak (i.e., 4.04 nm for N-500 and 5.50 nm for A-500). High-resolution TEM analysis further indicates that these CeO_2 NPs are single-crystalline (inset, Fig. 1b), with lattice spacings of 0.32 nm corresponding to the (111) planes of CeO_2. For comparison, single-crystalline spherical CeO_2 NPs (denoted as Ce-Sp), about 5 nm in size, were also prepared in this study using a typical wet precipitation method (see Fig. S4 for characterization) [34].

The Ce_{3d} XPS spectra of N-500 and A-500 (Fig. 1d(i)) closely resemble that of Ce-Sp, with a Ce^{3+}/Ce^{4+} ratio of 0.26 (see Fig. S5 for peak deconvolution). In contrast, the $Ce(NO_3)_3$-PVP mixture exhibits a significantly higher ratio of 1.30, indicating a successful transition from ionic Ce^{3+} to lattice Ce^{4+} in CeO_2 at elevated temperatures. This transition is also supported by the XPS O_{1s} spectra (Fig. 1d(ii)), which shows a change in the chemical environment of oxygen from NO_3^- in the mixture to lattice oxygen in CeO_2 for N/A-500. The N_{1s} XPS spectra further reveal that all nitrogen species in the mixture, particularly those from NO_3^-, were removed in A-500 (Fig. 1d(iii)). In contrast, in N-500, the nitrogen from NO_3^- and PVP was mostly retained and transformed into pyrrolic N and Ce—N species, likely due to the inert conditions used during synthesis (cf. oxidative conditions in air for A-500). The N_2 used for these inert conditions is unlikely to be the nitrogen source, as supported by passing argon instead during synthesis, which also yields samples in similar structure containing these N-related species (Fig. S6). Apart from the differences in the presence/absence of nitrogen-related species, we can conclude that the obtained N/A-500 samples exhibit high structural similarity, consisting of ultrasmall CeO_2 NPs (ca. 5 nm) densely populated within a porous carbon-based framework. Notably, this structure does not form when calcining $Ce(NO_3)_3$ or PVP (denoted as N/A-PVP) alone in N_2/air at 500 °C (Fig. S7).

3.2. Selective mimicking of POD and BOP

The POD-like activity of the samples was assessed by oxidizing colorless TMB to its blue product, TMB_{ox}, at 652 nm using UV–vis spectroscopy (Fig. 2a(i)). The results show that N-500 exhibited superior POD-like activity (Fig. 2a(ii)), while A-500, Ce-Sp, and control samples (i.e., $Ce(NO_3)_3$-PVP and N/A-PVP; see Fig. S8 for their raw spectra) demonstrated significantly reduced activity. The initial rate constant, k ($*10^{-3}$ min^{-1}), was 2.10 for N-500, over 10 times higher than A-500 (0.18), 3 times higher than Ce-Sp (0.63), and 25 times higher than the control samples (0.08) (Fig. 2a(iii); see Fig. S9 for kinetic fitting). Since the $Ce(NO_3)_3$-PVP mixture and N/A-PVP samples show negligible differences compared to the blank, it is concluded that neither the residual ionic Ce^{3+} nor the carbon-based framework in N/A-500 contributes to

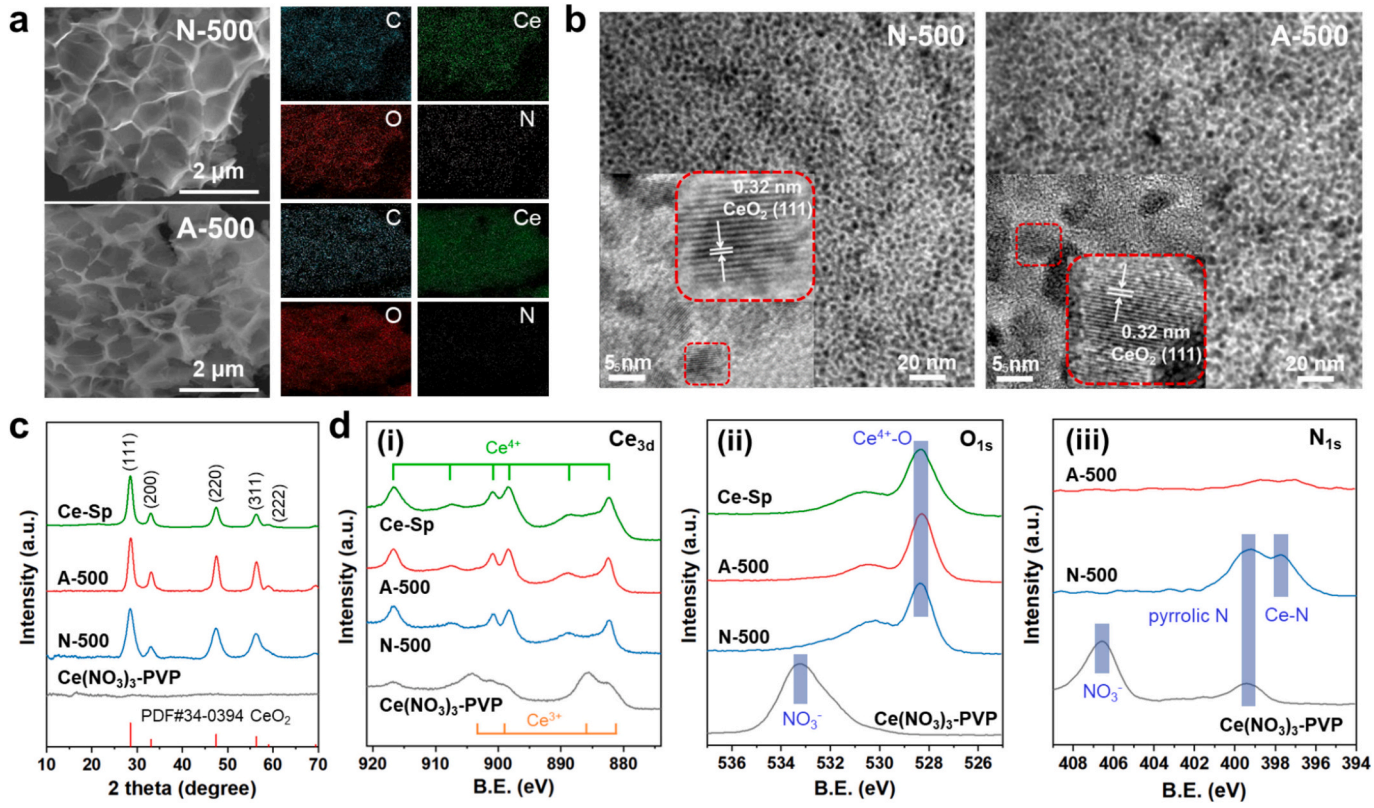

Fig. 1. (a) SEM images and elemental mapping; (b) TEM images and lattice analysis of N-500 and A-500. (c) XRD, and (d) XPS measurements of the samples.

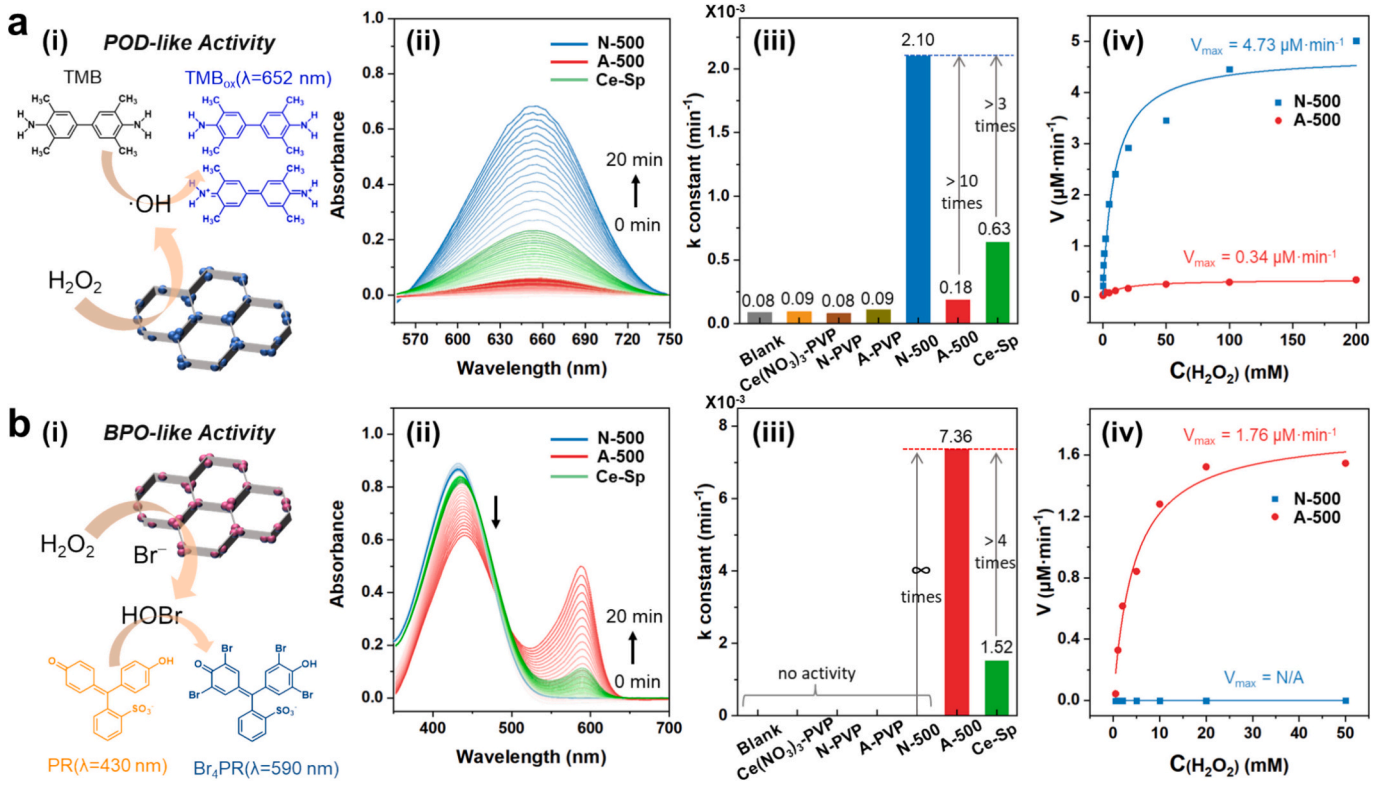

Fig. 2. Catalytic results showing (a) POD-like activity and (b) BPO-like activity of the samples, along with their corresponding (i) schematic illustrations, (ii) time-dependent UV–Vis spectra, (iii) calculated *k* constants, and (iv) performance with H_2O_2 concentrations.

the observed POD-like activity. Michaelis–Menten analysis was further conducted for N/A-500 to assess how their reaction rates vary with H_2O_2

concentration ([H_2O_2]). As shown in Fig. 2a(iv), N-500's reaction rate sharply increases, particularly at [H_2O_2] below 25 mM, reaching a maximum velocity (V_{max}) of 4.73 uM·min^{-1}. In contrast, A-500's reaction rate remains constant up to for 200 mM H_2O_2, with a significantly lower V_{max} of 0.34 uM·min^{-1}, consistent with the observed differences in their *k* constants (> 10 times).

To evaluate BPO-like activity, we monitored HOBr production through the bromination of phenol red (PR) to Br_4PR, which has a characteristic absorbance at 590 nm (Fig. 2b(i)). Notably, A-500 and Ce-Sp were the only active samples in this reaction (Fig. 2b(ii), see Fig. S10 for raw spectra), with A-500 exhibiting a *k* constant of 7.36 (*10^{-3} min^{-1}), more than 4 times higher than that of Ce-Sp (Fig. 2b(iii); see Fig. S11 for kinetic fitting). Since N-500 is inactive, the enhancement of A-500 is therefore infinite. These findings also confirm that neither the residual ionic Ce^{3+} nor the carbon-based framework in A-500 contributes to its BPO-like activity. Fig. 2b(iv) shows the reaction rate as a function of [H_2O_2] for N/A-500. As expected, N-500 remained inert, while A-500's reaction rate increases with elevated [H_2O_2], reaching a V_{max} of 1.76 μM·min^{-1}. Altogether, our synthetic method for CeO_2 nanozymes is not only straightforward but also enables precise control of H_2O_2 activation pathway via simple adjustments to the calcination atmosphere, achieving specificity akin to that of natural POD/ BPO enzymes (Fig. S12). The sample previously prepared under argon also displays exclusive POD-like activity, similar to that of N-500 (Fig. S13). Further comparing the performance of N/A-500 with Ce-Sp, it is evident that suppressing one enzymatic activity can effectively minimize interference from H_2O_2 competition, thereby intrinsically enhancing the activity of the other.

The effect of PVP molecular weight on synthesis and their POD-/BPO-like activities were further evaluated. The N/A-500 samples above were prepared using PVP with a molecular weight of 1,300,000. Additional samples were calcined at 500 °C using PVP with molecular weights of 10,000, 55,000, and 220,000 under N_2/air atmospheres (denoted as N/A-500(10*K*—220*K*)). The N-500 samples (N-500-10 K/55 K/220 K) reveal a honeycomb-like framework, with embedded CeO_2 NPs decreasing in size as PVP molecular weight increases (Fig. S14a), as evidenced by the broadening of XRD peaks (Fig. S14b). In contrast, the A-500 samples (A-500-10 K/55 K/220 K) show no porous structure but severe aggregation of CeO_2 NPs, consistent with their sharp diffraction peaks in the XRD patterns. These samples were subsequently assessed for their POD-/BPO-like activities (Fig. S15), with first-order kinetic fitting presented and compared in Fig. S16. For N-500-10 K/55 K/220 K, the *k* values for POD-like activity increase from 0.83 (10*K*) to 0.98 (55 K), and further to 1.62 (220*K*) as the molecular weight of PVP rises. This gradual enhancement is likely related to the reduced CeO_2 particle size achieved at higher PVP molecular weights. In contrast, A-500-10 K/55 K/220 K samples exhibit low *k* values for BPO-like activity ranging from 0.71 to 1.59, which can be attributed to severe aggregation. Altogether, the samples prepared with lower PVP molecular weights exhibit poorer POD-/BPO-like activity compared to the N/A-500 samples, which were prepared with a PVP molecular weight of 1,300,000 and used throughout this study.

3.3. The key species regulating H_2O_2 activation

In the literature, the mimicking of POD and BPO by CeO_2 nanozymes is often correlated to Ce^{3+}/Ce^{4+} ratios derived from XPS Ce_{3d} results [24–29,49]. However, this does not apply to N/A-500 (also for Ce-Sp), which have identical Ce^{3+}/Ce^{4+} ratios (Fig. S5) but exhibit distinct mimicking behaviors (Fig. 2). This discrepancy could be attributed to the limitations of Ce_{3d} XPS, which reveals only discrete oxidation states (Ce^{3+} or Ce^{4+}) and lacks the ability to report variations in Ce electron density influenced by its local environment [50,51]. For example, because nitrogen is less electronegative than oxygen, its presence in N-500 should alter the electronic structure of Ce sites that are solely coordinated by oxygen in A-500. However, this difference is not evident in their XPS Ce_{3d} spectra (Fig. 1d(i)). To resolve this, we employed ^{31}P nuclear magnetic resonance (NMR) using trimethylphosphine oxide (TMPO) as a surface probe [31]. This Lewis basic molecule can interact specifically with surface Lewis acidic Ce sites, where a stronger interaction results in a positive shift in ^{31}P resonances, enabling differentiation of Ce electron density across the samples. As shown in Fig. 3a, A-500 exhibits a more positive ^{31}P shift of 52.9 ppm compared to 48.6 ppm for N-500, revealing that the surface Ce sites in N-500 indeed have higher electron density. This increased electron density is attributed to the formation of Ce—N species in the sample, which can exert a greater influence on the Ce electronic structure than the dative bonding of pyrrolic N. Additionally, the negligible overlap of their ^{31}P signals (Fig. 3a) further indicates a distinct charge distribution of surface Ce sites in N/A-500. This distinction in Ce electron density may explain why they can activate H_2O_2 through a different pathway, enabling nearly 100% specificity in their POD-/BPO-like activity. In contrast, the surface Ce sites of Ce-Sp exhibit a ^{31}P signal centered at 51.8 ppm, with a broad distribution across that of N-500 and A-500 (Fig. 3a). This medium Ce electron density may thus allow H_2O_2 activation via both pathways, leading to the observed poor POD-like and BPO-like activities in the sample.

To further validate the above correlations, we explore how the electron densities of these Ce sites can lead to H_2O_2 activation through either distinct pathways or a combination of both (Scheme 1b). For POD mimicry (Fig. 2a), TMB acts as a color indicator for OH radicals. A similar trend in POD-like activity should also be observed for the samples using electron paramagnetic resonance (EPR) with 5,5-dimethyl-1-pyrroline *N*-oxide (DMPO) as a trapping agent. Indeed, a strong DMPO-OH signal with a 1:2:2:1 resonance intensity is detected for N-500, followed by Ce-Sp, while A-500 shows an intensity comparable to the blank (Fig. 3b). This confirms that the electron-rich Ce sites in N-500 can effectively reduce H_2O_2 to OH radicals, whereas the reaction is hindered in Ce-Sp and significantly suppressed in A-500 due to the decreasing electron density in their Ce sites (i.e., less able to reduce H_2O_2). Since OH radicals also decompose free H_2O_2, we further monitored the time-dependent concentration of H_2O_2 by tracking its characteristic absorption at 240 nm (ε = 39.4 M^{-1}·cm^{-1}). As shown in Fig. 3c (dash lines), [H_2O_2] gradually decreases for N-500, followed by Ce-Sp, while no decomposition is observed for A-500 over the same period. These findings confirm the radical-mediated POD-like activity of N-500 and Ce-Sp, where OH radicals oxidize not only TMB (Fig. 2a) and DMPO (Fig. 3b) but also free H_2O_2.

Although the Ce-peroxo species formed exclusively on A-500 (and partially on Ce-Sp) is unable to oxidize these substrates, it has been shown to selectively oxidize Br^- to produce HOBr [32]. To validate this, we tracked [H_2O_2] again for the samples in the presence of Br^-. Fig. 3c (solid lines) shows a significant decrease in [H_2O_2] for A-500 this time, followed by Ce-Sp, while no change for N-500 (cf. their cases without Br^-). The Br^--triggered [H_2O_2] decrease in A-500 can be inferred to the consumption of H_2O_2 through the reaction between Br^- and its Ce-peroxo species. In contrast, the negligible change in [H_2O_2] for N-500 after Br^- addition suggests the absence of these species in the sample. For Ce-Sp, the accelerated decrease in [H_2O_2] with Br^- indicates that its Ce sites can activate H_2O_2 via both radical and peroxo pathways. We further performed time-dependent Raman spectroscopy on A-500 to monitor the fate of H_2O_2, both in the absence and presence of Br^-. As shown in Fig. S17a, the O—O bond of free H_2O_2 exhibits a Raman signal at 875 cm^{-1}, while the additional shoulder at around 850 cm^{-1} is attributed to the Ce-peroxo species (or adsorbed H_2O_2) with an elongated O—O bond [52]. In the absence of Br^-, the intensity of both signals remains stable over time, suggesting that the Ce-peroxo species on A-500 cannot oxidize free H_2O_2. This finding aligns with the negligible H_2O_2 decomposition observed in the absence of Br^- (Fig. 3c). In contrast, H_2O_2 is rapidly consumed within 5 min in the presence of KBr (Fig. S17b), leading to the disappearance of the Raman signal at 875 cm^{-1} and a tiny signal from residual surface Ce-peroxo species at 850

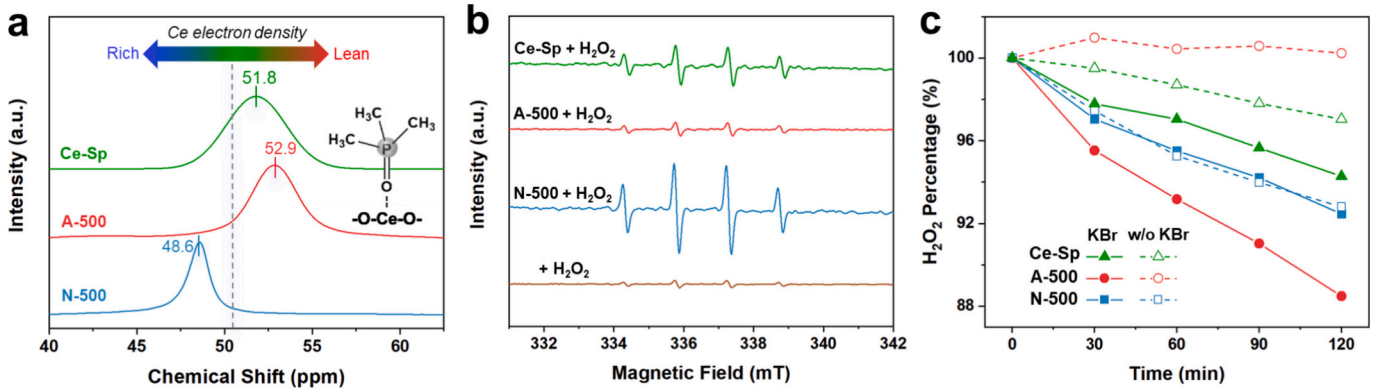

Fig. 3. (a) TMPO-assisted ^{31}P NMR spectra of the samples. (b) DMPO-assisted EPR monitoring the generation of OH radicals over the samples and (c) their time-dependent H_2O_2 decomposition in the absence (dash lines) and presence of KBr (solid lines).

cm^{-1}. This, along with the progressive production of HOBr by A-500 (Fig. 2b(ii)), confirms that the observed BPO-like activity is closely linked to the reaction between Br^- and surface Ce-peroxo species.

Overall, it is concluded that the exclusive POD-like activity of N-500 arises from the electron-rich Ce sites associated with the Ce—N species, which effectively reduce H_2O_2 to OH radicals. In contrast, A-500, prepared in air with electron-lean Ce sites, hinders H_2O_2 reduction and promotes the formation of Ce-peroxo species for Br^- oxidation, leading to selective BPO-like activity. For Ce-Sp, the medium electron density of its Ce sites enables H_2O_2 activation through both pathways, resulting in

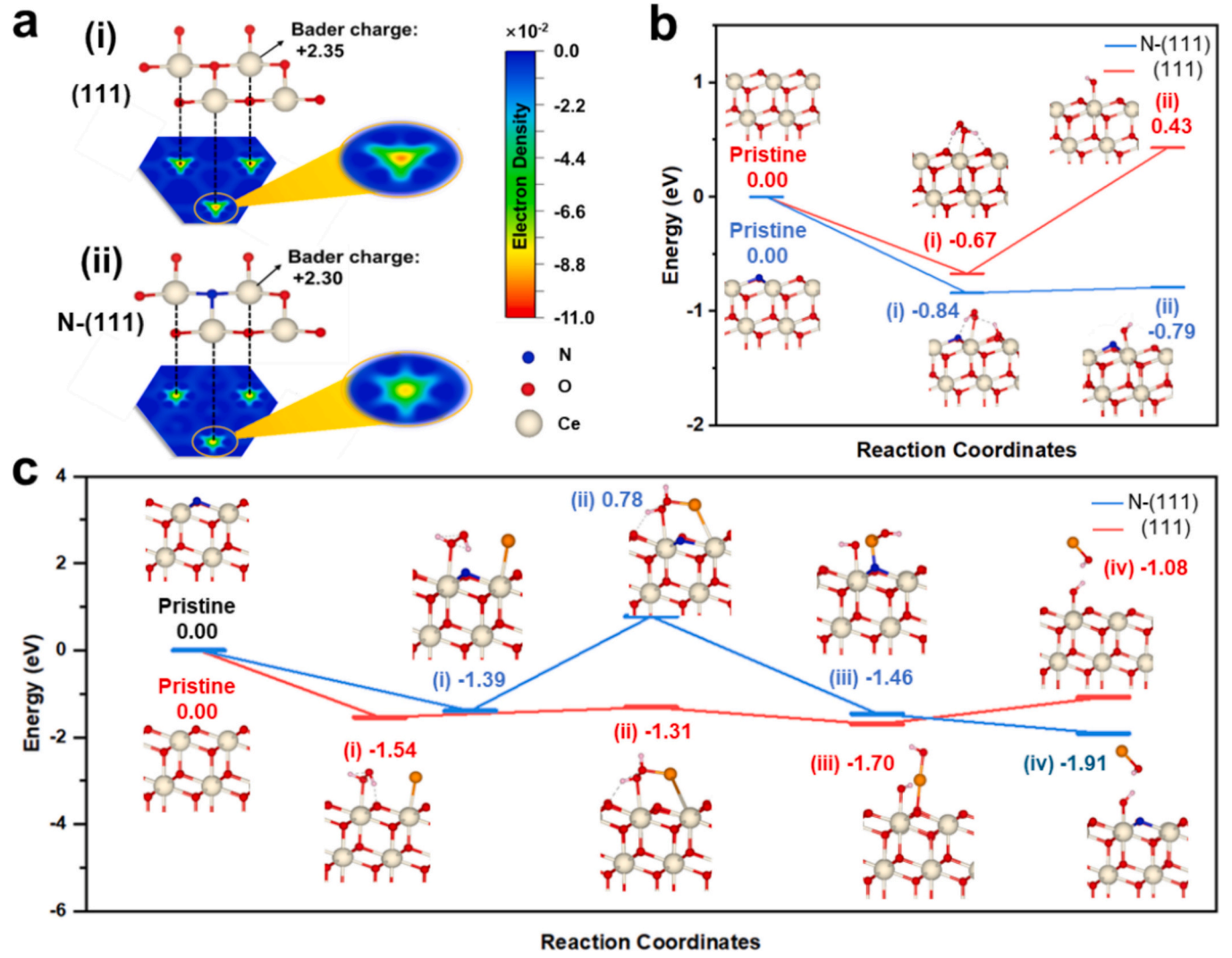

Fig. 4. (a) Top view of the CeO_2 (111) slabs before (i) and after (ii) replacing a surface oxygen by a nitrogen. Energy profiles showing (b) the formation of surface peroxo species and the release of an OH radical from pristine (111) and N-doped (111) surfaces, and (c) the energy profiles for forming O-bridged Br species and producing HOBr.

low POD-like and BPO-like activities due to a lack of specificity.

3.4. Theoretical insights

Since CeO_2 NPs in N/A-500 are enclosed by the (111) surface (Fig. 1b), we chose CeO_2(111) as a model surface to study the electronic effect of nitrogen on the surface Ce sites and its role in affecting H_2O_2 activation. For the pristine (111) surface (Fig. 4a(i)), the 7-coordinated surface Ce site, surrounded by oxygen atoms, exhibits a Bader charge of +2.35 |e|. However, when one of the surface oxygen atoms is replaced by a nitrogen atom (denoted as N-(111), Fig. 4a(ii)), the charge decreases to +2.30 |e|. This suggests an increase in electron density at the Ce sites on the N-(111) surface, which may thus facilitate H_2O_2 reduction compared to the pristine (111) surface. The projected density of states (PDOS) analysis was further performed to provide insights at orbital level. The PDOS of the outmost layer of Ce and O (or N) atoms at the pristine (111) and N-(111) was plotted in Fig. S18. The valence band (VB) and conduction band (CB) of pristine CeO_2 are predominantly composed of fully occupied O_{2p} orbitals and unoccupied Ce_{4f} orbitals, respectively. Upon nitrogen incorporation, N-(111) exhibits a narrower band gap compared to the pristine (111). Additionally, a distinctive feature of the spin-down electronic states localized near the Fermi level (where E-$E_f = 0$ eV) can be attributed to the hybridization between the Ce_{4f} and N_{2p} orbitals. The occupied states near the Fermi level exhibit high electron mobility, which is believed to make them favorable for electron transfer to H_2O_2, thus facilitating its reduction to OH radicals.

The stronger Lewis basicity of nitrogen (cf. oxygen) was also found to influence H_2O_2 adsorption and subsequent activation. As shown in Fig. 4b(i), H_2O_2 coordinates monodentately to Ce sites on both surfaces, exhibiting a stronger adsorption energy (E_{ad}) of −0.84 eV for N-(111) versus −0.67 eV for pristine (111). The difference in E_{ad} can be attributed to stronger hydrogen bonding between H_2O_2 hydrogen and lattice nitrogen (cf. lattice oxygen), which induces the transfer of another H_2O_2 hydrogen to the surface. Consequently, the generation of OH radicals is thermodynamically favorable on N-(111) at −0.79 eV (Fig. 4b(ii)), while this value is positive for pristine (111), with an E_{ad} of 0.43 eV, indicating that the process is more favorable on N-(111). However, when Br is co-adsorbed (Fig. 4c(i)), the nucleophilic attack by H_2O_2 oxygen on Br is hindered on N-(111) (Fig. 4c(ii)), preventing the formation of surface O-bridged Br species (Fig. 4c(iii)), which is the key intermediate for HOBr production [32], as further confirmed by the climbing image nudged-elastic band method (CI-NEB) calculations (Fig. S19). In contrast, these steps are thermodynamically favorable on pristine (111). The solvent effect (Fig. S20) and thermal corrections (e.g., free energy, Fig. S21) were also considered for the key intermediate species in the calculations for both POD and BPO pathways, with no significant changes observed in their overall trends. Therefore, these variations are believed to have a minor impact on our simulation.

Altogether, the simulation results suggest that the presence of surface nitrogen on N-(111) surface (i.e., N-500) not only enhances the electron density of the surrounding Ce sites but also assists the reduction of H_2O_2 through its Lewis basicity. However, these effects impede the surface reaction between H_2O_2 and Br, making the production of HOBr more favorable on the pristine (111) surface (i.e., A-500).

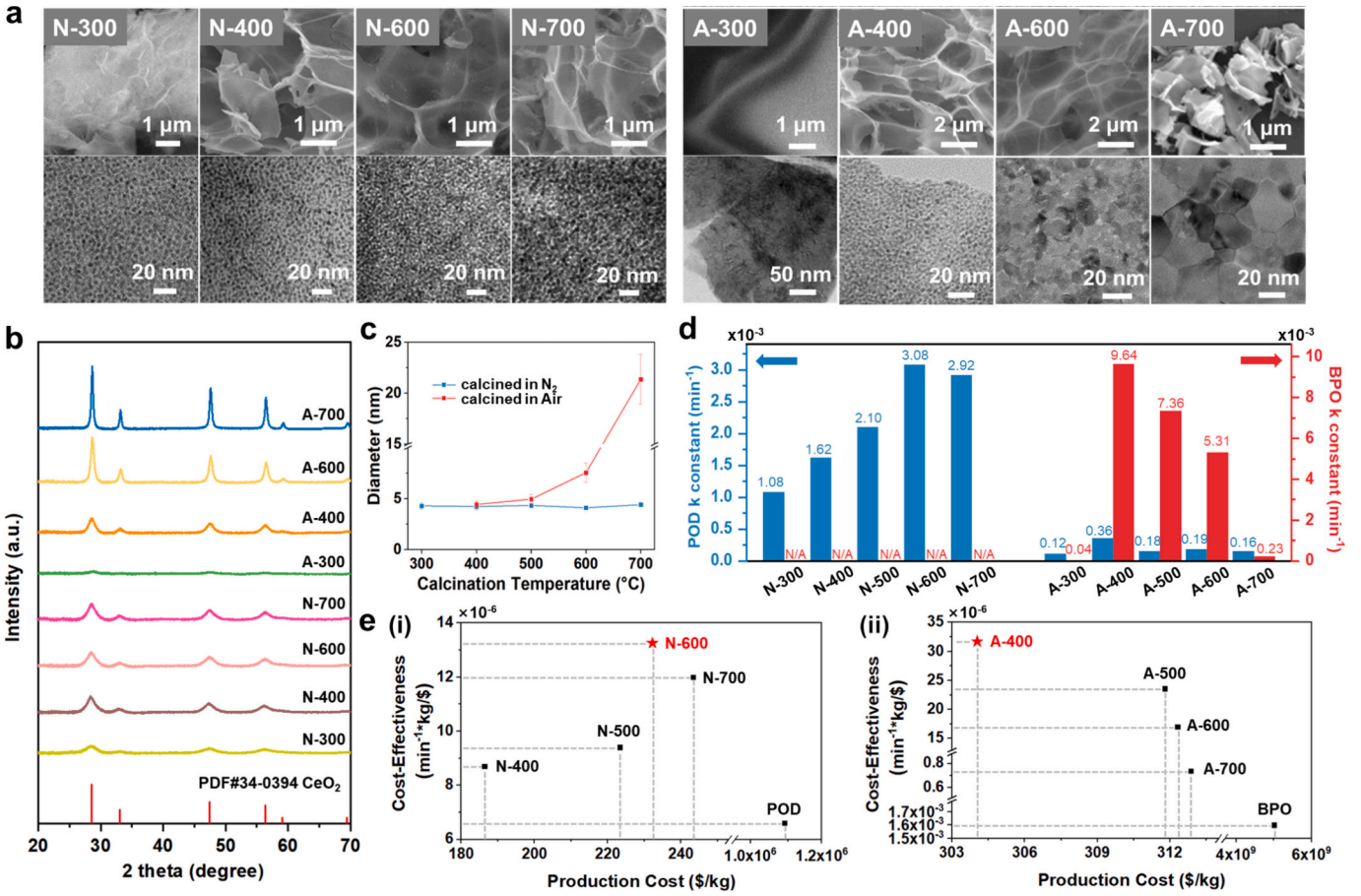

Fig. 5. (a) SEM (top) and TEM (bottom) images, and (b) XRD spectra of the samples obtained at elevated temperature in N_2/air. (c) Size distribution of CeO_2 NPs in these samples, and (d) their corresponding k constants in POD-like activity (blue column) and BPO-like activity (red column). (e) Estimated production costs and cost-effectiveness for (i) N_2-calcined and (ii) air-calcined samples.

3.5. Temperature effect, cost-effectiveness, and stability

The effect of calcination temperature on the sample prepared by our method was further explored. For N_2-prepared samples (N-300/400/600/700), SEM images reveal a honeycomb-like framework across temperatures from 300 °C to 700 °C (Fig. 5a). However, air-prepared samples (A-300/400/600/700) exhibit this structure up to 400 °C and collapsed by 700 °C. TEM images and XRD spectra confirmed the presence of CeO_2 NPs in these samples (Fig. 5b). In N_2, the NPs averaged about 4.3 nm in size across temperatures (Fig. 5c; see Fig. S22 for statistics), as supported by their consistent XRD peak width. In contrast, under air conditions, CeO_2 NPs were barely formed at 300 °C and began to appear above 400 °C, with sizes increasing from 4.5 nm for A-400 to 7.2 nm for A-600 (see Fig. S23 for statistics), and sharply rising to 21.1 nm for A-700 due to the decomposition of the carbon-based framework. This trend is also reflected in the increasing intensity of their XRD peaks at elevated temperatures. Thermogravimetric analysis (TGA) of the Ce $(NO_3)_3$-PVP mixture indicates greater weight loss in air than in N_2 above 300 °C (Fig. S24), which can be attributed to enhanced decomposition under oxidative conditions, leading to distinct growth kinetics for the N_2/air-prepared samples.

These samples were then accessed for their POD-like (Fig. S25) and BPO-like (Fig. S26) activities, with first-order kinetic fitting presented in Fig. S27. The *k* constants summarized in Fig. 5d indicate that N_2-prepared samples exhibit only POD-like activity, while those prepared in air show dominant BPO-like activity. This confirms again that the specificity of samples prepared by our method is dictated by the calcination atmosphere, while temperature only influences the level of activity. As expected, both N_2- (Fig. S28) and air-prepared samples (Fig. S29) exhibit similar Ce^{3+}/Ce^{4+} ratios (0.26–0.27 for samples above 400 °C), with only N_2-prepared samples displaying a Ce—N signal (Fig. S30). The presence/absence of this signal in our samples, as discussed, is crucial in determining whether they exhibit POD- or BPO-like activity. Regarding POD-like activity, although the sizes of CeO_2 NPs in the N_2-prepared samples are similar (Fig. 5c), the activity increases with higher calcination temperatures, reaching a plateau above 600 °C (Fig. 5d). This trend closely aligns with the increasing Ce concentration in the samples (Table S2), suggesting an increased number of CeO_2 NPs per gram of sample, which also peaks at temperatures above 600 °C. In contrast, for air-prepared samples, the BPO-like activity reaches its peak at 400 °C (Fig. 5d), coinciding with the initial formation of CeO_2 NPs (cf. 300 °C). Although the concentration of Ce remaining in these samples also increases with calcination temperature (Table S2), the gradual decline in BPO-like activity at temperatures above 400 °C can primarily be attributed to the increased particle size of CeO_2 NPs, particularly at 700 °C (Fig. 5c).

By assessing the quantities of raw materials used, the conversion efficiencies of the samples can be determined (Table S3) to calculate their production cost (Table S4). The estimated cost per kilogram for N_2-prepared samples ranges from $180 to $250 (Fig. 5e(i)), while air-prepared samples are higher at around $310 (Fig. 5e(ii)) due to lower mass preservation (Fig. S24). These costs are significantly lower than those of commercial POD (~$1 million per kilogram) and BPO (~$5 billion per kilogram), which require specific raw materials and complex production processes (Fig. S31). To further evaluate cost-effectiveness, we normalized their *k* constants by production cost (Table S4). As also shown in Fig. 5e, N-600 and A-400 exhibited the highest cost-effectiveness compared to other samples and natural enzymes, indicating greater economic viability as POD and BPO mimetics for large-scale production. Both optimal samples also demonstrated superior pH/thermal stability, maintaining high catalytic activity under varying pH (Fig. 6a) and temperature (Fig. 6b) conditions compared to their natural counterparts. In terms of shelf stability, negligible changes were observed in their porous framework and the sizes and crystal structure of CeO_2 NPs (Fig. S32) after 6 months of storage under ambient conditions, resulting in maintained POD-/BPO-like activity (Fig. S33). Regarding recyclability, they preserved about 90% of their activity after five catalytic cycles (Fig. S34), with the 10% decrease likely due to sample loss

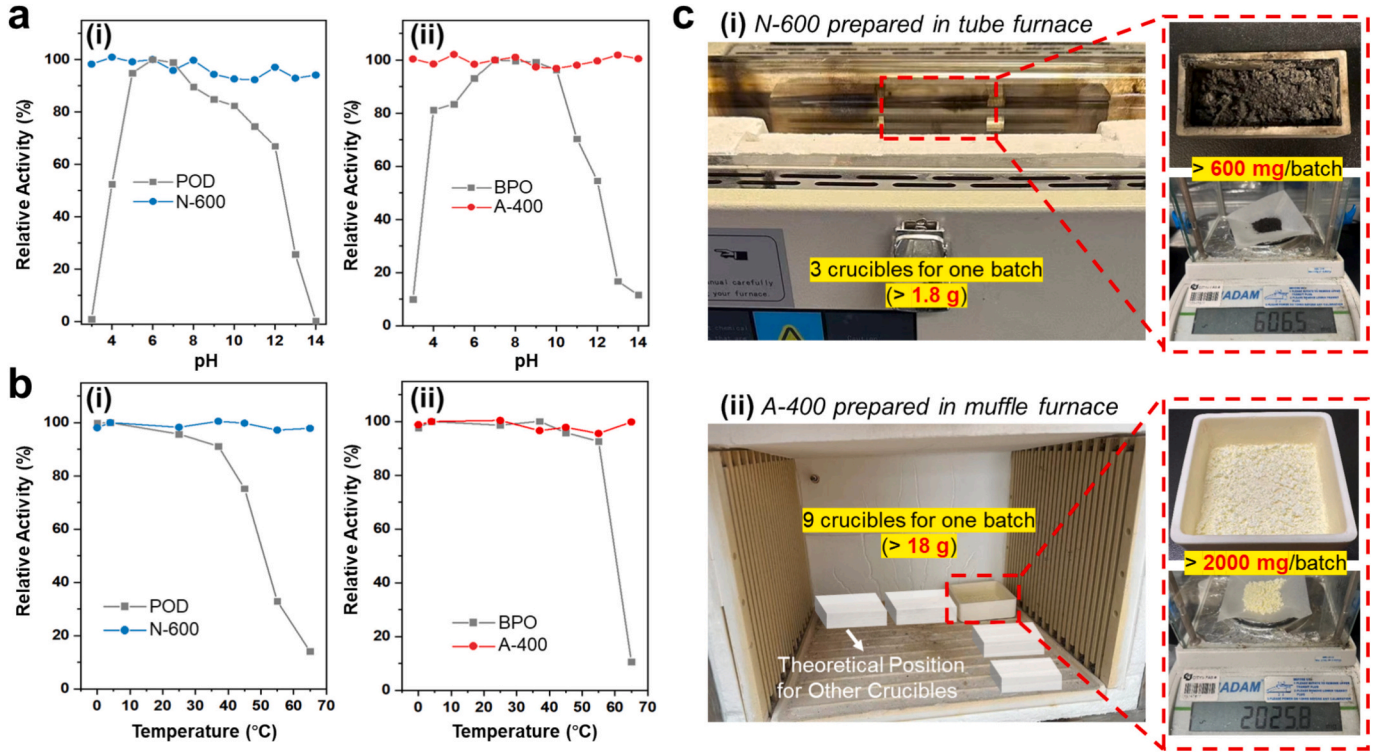

Fig. 6. (a) pH and (b) temperature stability tests for (i) N-600 and (ii) A-400, along with their comparisons to POD [pH 6 and 4 °C set as 100%] and BPO [pH 7 and 4 °C set as 100%], respectively. (c) Equipment used for the preparation of (i) N-600 and (ii) A-400 and their quantities produced in each crucible along with the total production for each run.

during collection. In our laboratory, N-600 can be prepared at ca. 1.8 g per run (about 600 mg per crucible across three crucibles, Fig. 6c(i)), while A-400 yields over 18 g per run, with around 2 g obtained from each crucible (Fig. 6c(ii)). We are currently testing larger furnaces to enhance production quantities, aiming to integrate this approach with continuous flow reactors for mass production.

3.6. Glucose detection and anti-bacterial/fouling applications

To highlight the importance of surface Ce sites with proper electron density for H_2O_2 activation via the targeted pathway for optimal POD/BPO-related performance, N-600 and A-400—exhibiting the highest POD-/BPO-like activities—were selected for comparison in glucose detection and antibacterial/fouling applications. In diabetes research, glucose detection kits typically utilize an enzymatic assay involving glucose oxidase (GO*x*) and POD (Fig. 7a). GO*x* first oxidizes glucose to produce H_2O_2, which then reacts with POD to generate TMB_{ox}, resulting in a color change. When POD was replaced by N-600, TMB can be effectively oxidized to TMB_{ox}, showing a notable intensity increase at 652 nm as glucose concentrations rose from 1 μM to 2000 μM (Fig. 7b). In contrast, A-400, which has negligible POD-like activity, exhibited minimal response to glucose concentrations. While both samples demonstrated a linear range of 5–100 μM (Fig. 7c; see enlarged for A-400 in Fig. S35), N-600 showed nearly 30 times greater sensitivity and over 20 times lower limit of detection (LOD) compared to A-400 (Table S5). This result underscores the need for surface Ce sites to possess the highest possible electron density to accelerate H_2O_2 reduction for OH radicals, thereby enhancing performance in POD-related applications with pristine CeO_2. N-600 also displayed high selectivity for glucose among various competing substances at concentrations ten times higher (Fig. 7d). We further evaluated the potential of substituting POD with N-600 in enzymatic assays using glucose levels from various serum samples. The results summarized in Table S6 indicate that N-600 can achieve ~100% recoveries, comparable to that of a commercial glucose monitoring device (Fig. 7e). The performance of N-600 was compared with common transition metal oxides in Table S7. While N-600 has a narrower linear range than the 3d transition metal oxides (entries 1–7), it achieves a superior LOD compared to most. When compared to CeO_2 nanozymes reported in the literature (entries 8–10), our sample outperforms them, likely due to its ultrasmall particle sizes and electron-rich Ce sites, which can all activate H_2O_2 via radical pathway, contributing to the POD-like activity.

Despite the common use of POD [53]/BPO [26–29]-like nanozymes for antibacterial applications, their effectiveness in bacterial killing is rarely compared. Thus, N-600 and A-400, both exhibiting ~100% specificity for POD/BPO mimicking, were used to assess which is more effective in eliminating bacteria. Fig. 7f shows their antibacterial activity against *Escherichia coli* (*E. coli*) under different conditions, with the colony images and corresponding SEM images displayed in Fig. 7g. Bacterial survival rates exceed 90% with treatment using H_2O_2, N-600, or A-400 alone. The viability of N-600 decreases to 83% in the presence of H_2O_2 due to its POD-like activity converting H_2O_2 into OH radicals. Surprisingly, A-400's viability remains unchanged after H_2O_2 addition, likely due to the formation of surface peroxo species that consume free H_2O_2 and reduce cytotoxicity. Upon further addition of Br^-, N-600 shows minimal change in antibacterial activity (from 83% to 80%), while A-400's viability drops significantly to about 4% (from 94%), with no intact bacteria observed. The antibacterial efficacy of A-400 was further compared with BPO nanozymes reported in the literature (Table S8). Although nearly half of its mass consists of inactive carbon framework, it demonstrated the highest antibacterial performance at the lowest catalyst concentration used. This can be attributed not only to the ultrasmall CeO_2 NPs but also to their electron-deficient Ce sites, all of which can activate H_2O_2 via peroxo pathway, contributing to the BPO-like activity. For antifouling testing, both N-600 and A-400 samples were applied to steel slices during preparation (Fig. 7h(i)). Successful

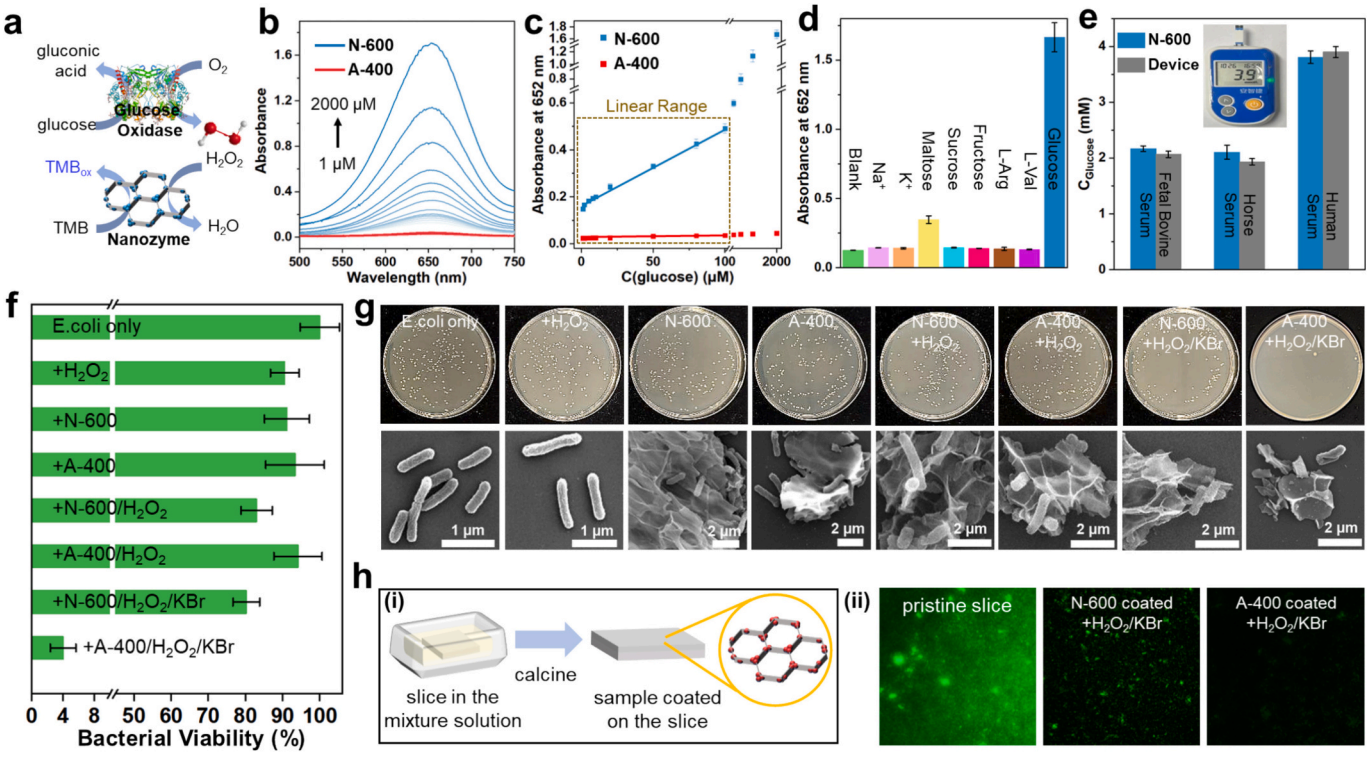

Fig. 7. (a) Schematic illustration of coupled enzyme reactions for glucose detection. (b) UV–vis spectra and (c) response of N-600 and A-400 as POD mimetics to glucose concentrations. (d) Selectivity test of N-600 as POD mimetic and (e) comparison of glucose levels in serum samples with commercial glucose monitoring device. (f) Bacterial viability assessment of *E. coli* under different conditions and (g) the corresponding digital photographs and SEM images. (h) (i) The preparation of slices and (ii) their exposure to GFP-*E. coli* suspensions.

coating is demonstrated by SEM images and the corresponding signals of C, Ce, and O in the coated slices (Fig. S36). The antifouling effect was assessed by immersing the slices in a suspension of GFP-*E. coli* (green fluorescent protein-expressing *E. coli*) with Br^- and H_2O_2 at 37 °C for a week. Confocal images in Fig. 7h(ii) reveal that the pristine slice exhibited complete green emission, indicating a high density of live GFP-*E. coli*. The N-600 coated slice slightly inhibited biofilm growth, while no green emission was observed on the A-400 coated slice, indicating that BPO-like activity is more effective than POD-like activity for anti-bacterial/fouling applications. These findings again highlight the significance of surface Ce sites having the lowest possible electron density to promote the formation of Ce-peroxo for HOBr production, thereby enhancing performance in BPO-related applications with pristine CeO_2.

4. Conclusions

We present a facile method to prepare ultrasmall CeO_2 NPs within a carbon-based framework by calcining a $Ce(NO_3)_3$-PVP mixture at elevated temperatures. By controlling the calcination atmosphere, we achieve near-perfect mimicry of POD/BPO-like activities in the resulting CeO_2 nanozymes. This approach, along with the elimination of purification steps, ensures better cost-effectiveness for mass production compared to natural enzymes. Surface and mechanistic studies reveal that the exclusive POD-like activity of N_2-prepared samples arises from the electron-rich Ce sites associated with Ce—N species, which effectively reduce H_2O_2 to OH radicals. In contrast, air-prepared samples lack this species, resulting in electron-lean Ce sites that cannot reduce H_2O_2 but instead promote the formation of Ce-peroxo species. These species specifically oxidize Br^- to HOBr, leading to dominant BPO-like activity. Additionally, we demonstrated that the dual mimicking activities commonly observed in CeO_2 nanozymes (i.e., Ce-Sp here) stem from their medium electron density, which slowly activates H_2O_2 through both pathways. These findings suggest that suppressing one enzymatic activity can effectively reduce interference from H_2O_2 competition, thereby intrinsically enhancing the activity of the other. Finally, the optimized samples, N-600 and A-400, were used in glucose detection and antibacterial/fouling applications to highlight the importance of specificity control for optimal performance. Since no nanozyme or single-atom nanozymes have yet achieved such reaction specificity and scalability concurrently, this work marks a significant advancement in the field and is expected to guide future development for practical use.

CRediT authorship contribution statement

Tianqi Cheng: Writing – original draft, Investigation, Formal analysis, Data curation. **Bo Yuan:** Writing – review & editing, Writing – original draft, Investigation, Formal analysis, Data curation. **Chao Zhao:** Writing – original draft, Investigation, Formal analysis, Data curation. **Zicong Tan:** Methodology, Investigation, Formal analysis, Data curation. **Xinyu Wu:** Methodology, Investigation, Data curation. **Jian Lin Chen:** Resources, Conceptualization. **Juan Liu:** Supervision, Resources. **Yufei Zhao:** Resources, Conceptualization. **Hui Wei:** Writing – original draft, Investigation, Formal analysis, Conceptualization. **Yung-Kang Peng:** Writing – review & editing, Writing – original draft, Supervision, Investigation, Formal analysis, Conceptualization.

Declaration of competing interest

The authors declare that they have no known competing financial interests or personal relationships that could have appeared to influence the work reported in this paper.

Acknowledgements

The authors would like to thank the financial support from the Hong Kong Research Grants Council (CityU 11300524), CityU Strategic Research Grant (7006002), the Science and Technology Projects of Guangzhou (2025A04J4574) and Young Innovative Talents of Guangdong Regular Higher Education Institutions (2025KQNCX061). Open Access made possible with partial support from the Open Access Publishing Fund of the City University of Hong Kong.

Appendix A. Supplementary data

Supplementary data to this article can be found online at https://doi.org/10.1016/j.cej.2026.172970.

Data availability

Data will be made available on request.

References

[1] H. Wei, E. Wang, Nanomaterials with enzyme-like characteristics (nanozymes): next-generation artificial enzymes, Chem. Soc. Rev. 42 (2013) 6060–6093.
[2] Y. Huang, J. Ren, X. Qu, Nanozymes: classification, catalytic mechanisms, activity regulation, and applications, Chem. Rev. 119 (2019) 4357–4412.
[3] J. Wu, X. Wang, Q. Wang, et al., Nanomaterials with enzyme-like characteristics (nanozymes): next-generation artificial enzymes (II), Chem. Soc. Rev. 48 (2019) 1004–1076.
[4] D. Jiang, D. Ni, Z.T. Rosenkrans, et al., Nanozyme: new horizons for responsive biomedical applications, Chem. Soc. Rev. 48 (2019) 3683–3704.
[5] Y. Zhang, G. Wei, W. Liu, et al., Nanozymes for nanohealthcare, Nat. Rev. Methods Primers 4 (2024) 36.
[6] K. Wang, X. Meng, X. Yan, K. Fan, Nanozyme-based point-of-care testing: revolutionizing environmental pollutant detection with high efficiency and low cost, Nano Today 54 (2024) 102145.
[7] L. Yang, X. Xu, Y. Song, J. Huang, H. Xu, Research Progress of nanozymes in colorimetric biosensing: classification, activity and application, Chem. Eng. J. 487 (2024) 150612.
[8] H. Wei, L. Gao, K. Fan, E. Dong, X. Yan Wang, et al., Nanozymes: a clear definition with fuzzy edges, Nano Today 40 (2021) 101269.
[9] Y. Lyu, P. Scrimin, Mimicking enzymes: the quest for powerful catalysts from simple molecules to nanozymes, ACS Catal. 11 (2021) 11501–11509.
[10] M. Zandieh, J. Liu, Nanozymes: definition, activity, and mechanisms, Adv. Mater. 36 (2024) 2211041.
[11] H. Fan, R. Zhang, K. Fan, L. Gao, X. Yan, Exploring the specificity of nanozymes, ACS Nano 18 (2024) 2533–2540.
[12] G. Wei, S. Liu, Y.-K. Peng, H. Wei, On the specificity of nanozymes: a perspective, Chin. J. Chem. 42 (2024) 1515–1522.
[13] T.S. Baker, M.J. Perry, I.M. Fleming, "Binding Assay Device" Patent US5604110A, 1997.
[14] R. Wever, H.L. Dekker, J.W.P.M. Van Schijndel, E.G.M. Vollenbroek, "Antifouling Paint Containing Haloperoxidase and Method to Determine Halide" Patent WO/1995/027009, 1995.
[15] B. Yuan, H.-L. Chou, Y.-K. Peng, Disclosing the origin of transition metal oxides as peroxidase (and catalase) mimetics, ACS Appl. Mater. Interfaces 14 (2022) 22728–22736.
[16] Y. Qiu, B. Yuan, H. Mi, J.-H. Lee, S.-W. Chou, Y.-K. Peng, An atomic insight into the confusion on the activity of Fe_3O_4 nanoparticles as peroxidase mimetics and their comparison with horseradish peroxidase, J. Phys. Chem. Lett. 13 (2022) 8872–8878.
[17] J. Zhang, T.-S. Wu, H.V. Thang, et al., Cluster nanozymes with optimized reactivity and utilization of active sites for effective peroxidase (and oxidase) mimicking, Small 18 (2022) 2104844.
[18] Y. Cai, Z. Xiao, T. Cheng, et al., Facile gram-scale production of Cu/Cu_2O core/shell nanoparticles densely embedded in a porous carbon framework for cost-effective peroxidase mimicking, ACS Appl. Mater. Interfaces 17 (2025) 37577–37585.
[19] G. Sun, M.M.-J. Li, K. Nakagawa, et al., Bulk-to-nano regulation of layered metal oxide gears H_2O_2 activation pathway for its stoichiometric utilization in selective oxidation reaction, Appl. Catal. B 313 (2022) 121461.
[20] L. Tian, Y.-S. Liao, J.-P. Chou, et al., Facet-dependent Peroxo species regulate product distribution and H_2O_2 utilization in CeO_2-catalyzed aniline oxidation, J. Mater. Chem. A 11 (2023) 14034–14042.
[21] G. Sun, Q. Wang, Y.-S. Liao, et al., Manipulating the H_2O_2 reactivity on pristine anatase TiO_2 with various surface features and implications in oxidation reactions, J. Phys. Chem. Lett. 15 (2024) 11620–11628.
[22] K. Herget, P. Hubach, S. Pusch, et al., Haloperoxidase mimicry by CeO_{2-x} nanorods combats biofouling, Adv. Mater. 29 (2017) 1603823.
[23] T. Cheng, X. Wu, Y. Qiu, et al., Spatially decoupled H_2O_2 activation pathways and multi-enzyme activities in rod-shaped CeO_2 with implications for facet distribution, Small 20 (2024) 2401032.
[24] Z. Tian, J. Li, Z. Zhang, et al., Highly sensitive and robust peroxidase-like activity of porous nanorods of ceria and their application for breast cancer detection, Biomaterials 59 (2015) 116–124.

[25] J. Zhang, Z. Tan, W. Leng, et al., Chemical state tuning of surface Ce species on pristine CeO_2 with 2400% boosting in peroxidase-like activity for glucose detection, Chem. Commun. 56 (2020) 7897.
[26] X. He, F. Tian, J. Chang, et al., Haloperoxidase mimicry by CeO_2-x Nanorods of different aspect ratios for antibacterial performance, ACS Sustain. Chem. Eng. 8 (2020) 6744–6752.
[27] F. Cao, M. Zhang, K. Yang, et al., Single crystalline CeO_2 nanotubes, Nano Res. 14 (2021) 715–719.
[28] Z. Zhou, S. Li, G. Wei, et al., Cerium-based metal–organic framework with intrinsic haloperoxidase-like activity for antibiofilm formation, Adv. Funct. Mater. 32 (2022) 2206294.
[29] D. Su, X. He, J. Zhou, C. Yuan, X. Bai, Facet-dependent Haloperoxidase-like activities of CeO_2 nanoparticles contribute to their excellent biofilm formation suppression abilities, J. Hazard. Mater. 465 (2024) 133433.
[30] Y.-K. Peng, H.L. Chou, S.-C.E. Tsang, Differentiating surface titanium chemical states of anatase TiO_2 functionalized with various groups, Chem. Sci. 9 (2018) 2493–2500.
[31] Z. Tan, G. Li, H.-L. Chou, et al., Differentiating surface Ce species among CeO_2 facets by solid-state NMR for catalytic correlation, ACS Catal. 10 (2020) 4003–4011.
[32] B. Yuan, Z. Tan, Q. Guo, et al., Regulating the H_2O_2 activation pathway on a well-defined CeO_2 nanozyme allows the entire steering of its specificity between associated enzymatic reactions, ACS Nano 17 (2023) 17383–17393.
[33] Y. Qiu, T. Cheng, B. Yuan, T.Y. Yip, C. Zhao, J.-H. Lee, S.-W. Chou, J.L. Chen, Y. Zhao, Y.-K. Peng, One-pot and gram-scale synthesis of Fe-based Nanozymes with tunable O_2 activation pathway and specificity between associated enzymatic reactions, Small 21 (2025) 2408609.
[34] Y. Hu, X.J. Gao, Y. Zhu, et al., Nitrogen-doped carbon nanomaterials as highly active and specific peroxidase mimics, Chem. Mater. 30 (2018) 6431–6439.
[35] M. Li, J. Chen, W. Wu, Y. Fang, S. Dong, Oxidase-like MOF-818 Nanozyme with high specificity for catalysis of catechol oxidation, J. Am. Chem. Soc. 142 (2020) 15569–15574.
[36] M.S. Kim, J. Lee, H.S. Kim, A. Cho, K.H. Shim, et al., Heme cofactor-resembling Fe–N single site embedded graphene as nanozymes to selectively detect H_2O_2 with high sensitivity, Adv. Funct. Mater. 30 (2020) 1905410.
[37] Y. Wang, G. Jia, X. Cui, et al., Coordination number regulation of molybdenum single-atom nanozyme peroxidase-like specificity, Chem 7 (2021) 436–449.
[38] Q. Zhou, H. Yang, X. Chen, et al., Cascaded nanozyme system with high reaction selectivity by substrate screening and channeling in a microfluidic device, Angew. Chem. Int. Ed. 61 (2022) e202112453.
[39] S.V. Somerville, Q. Li, J. Wordsworth, S. Jamali, M.R. Eskandarian, R.D. Tilley, J. J. Gooding, Approaches to improving the selectivity of nanozymes, Adv. Mater. 36 (2024) 2211288.
[40] P. Giannozzi, S. Baroni, N. Bonini, et al., QUANTUM ESPRESSO: a modular and open-source software project for quantum simulations of materials, J. Phys. Condens. Matter 21 (2009) 395502.
[41] P. Giannozzi, O. Andreussi, T. Brumme, et al., Advanced capabilities for materials modelling with quantum ESPRESSO, J. Phys. Condens. Matter 29 (2017) 465901.
[42] G. Prandini, Precision and efficiency in solid-state pseudopotential calculations, npj Comput. Mater. 4 (2018) 72.
[43] P. Giannozzi, O. Baseggio, P. Bonfà, et al., Quantum ESPRESSO toward the Exascale, J. Chem. Phys. 152 (2020) 154105.
[44] J.P. Perdew, K. Burke, M. Ernzerhof, Generalized gradient approximation made simple, Phys. Rev. Lett. 77 (1996) 3865–3868.
[45] C.L. Muhich, Re-evaluating CeO_2 expansion upon reduction: noncounterpoised forces, not ionic radius effects, are the cause, J. Phys. Chem. C 121 (2017) 8052–8059.
[46] J. Hubbard, Electron correlations in narrow energy bands, Proc. R. Soc. Lond. A 276 (1963) 238–257.
[47] N.G. Hörmann, Z. Guo, F. Ambrosio, et al., Absolute band alignment at semiconductor-water interfaces using explicit and implicit descriptions for liquid water, npj Comput. Mater. 5 (2019) 100.
[48] A. Togo, L. Chaput, T. Tadano, et al., Implementation strategies in phonopy and phono3py, J. Phys. Condens. Matter 35 (2023) 353001.
[49] Y. Ma, Z. Tian, W. Zhai, Y. Qu, Insights on catalytic mechanism of CeO_2 as multiple nanozymes, Nano Res. 15 (2022) 10328–10342.
[50] Z. Tan, T.-S. Wu, Y.-L. Soo, et al., Unravelling the true active site for CeO_2-catalyzed dephosphorylation, Appl. Catal. B 264 (2020) 118508.
[51] L. Tian, Z. Tan, Q. Wang, et al., Cerium coordination-dependent surface intermediates regulate activity in dimethyl carbonate synthesis from CO_2 and methanol, Appl. Catal. B 336 (2023) 122914.
[52] Z. Tan, J. Zhang, Y.-C. Chen, et al., Unravelling the role of structural geometry and chemical state of well-defined oxygen vacancies on pristine CeO_2 for H_2O_2 activation, J. Phys. Chem. Lett. 11 (2020) 5390–5396.
[53] L. Mei, S. Zhu, Y. Liu, et al., An overview of the use of nanozymes in antibacterial applications, Chem. Eng. J. 418 (2021) 129431.